Design of Edge-Enhanced Coil Structure to Obtain Constant Mutual Inductance With Horizontal Misalignment in Wireless Power Transfer Systems of Electric Vehicles

Zhongqi LI, Zhongbang CHEN, Minsheng YANG, Yu CHENG, Xinbo XIONG, and Shoudao HUANG

***Abstract*—Horizontal misalignment to the *Y* and *X*-axes can be as much as half the side length of a transmitting resonant coil or 10 cm for both dynamic and static wireless power transfer (DSWPT) systems. Misalignment to the *Y*-axis and *X*-axis may cause DSWPT systems to malfunction due to fluctuations in mutual inductance. In this paper, a structure of edge-enhanced coil (EEC) is proposed. The mutual inductance expression of the EEC structure is then established. Moreover, the variation of the mutual inductance of the EEC structure is obtained based on the mutual inductance expression. The study demonstrates that the mutual inductance of the EEC structure can be increased while reducing its fluctuation. The problem that quasi-constant mutual inductance is obtained at the expense of mutual inductance value is solved. Therefore, the high transmission efficiency of DSWPT systems can be obtained, and the transmission efficiency and output power can be maintained almost constant with the misalignment to the *Y*-axis or *X*-axis. The calculated, simulated, and measured results validating the effectiveness of the EEC structure are shown.**

***Index Terms*—Coil structure, mutual inductance optimization, quasi-constant mutual inductance, wireless power transfer.**

I. Introduction

WIRELESS power transfer (WPT) technology is receiving increasing attention because of the convenience and safety of this technology [1]–[3]. This technology is widely used in electric vehicles (EVs) [4], automatic guided vehicles (AGVs) [5], [6], underwater vehicles (UVs) [7], [8], and drones [9], [10]. The advantage of WPT technology is that EVs can be charged while on the road using a dynamic WPT system, eliminating the need for batteries. At the same time, the static WPT technology provides smart charging services for EVs at home or office. Therefore, a set of coil structure should be used to simultaneously satisfy the dynamic and static WPT system requirements of EVs.

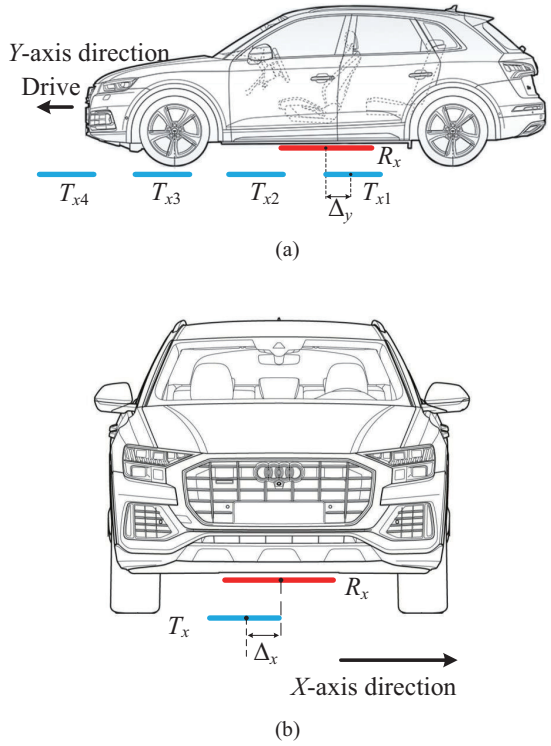

Fig. 1. Schematic diagram of wireless charging systems of EVs. (a) Dynamic wireless charging systems of EVs with misalignment along the *Y*-axis. (b) Static wireless charging systems of EVs with misalignment along the *X*-axis.

However, the unavoidable horizontal misalignment along the *Y*-axis and *X*-axis causes a change of the mutual inductance (MI) between the transmitting and receiving coils in the WPT system. The horizontal misalignment along the *Y*-axis may reach half the side length of a transmitting resonance coil in a dynamic WPT system for EVs, as shown in Fig. 1(a). According to SAE J2954, in a static wireless charging system for electric vehicles, the horizontal misalignment along the *Y*-axis and the *X*-axis can reach a least 7.5 cm and 10 cm, respectively, as shown in Fig. 1(b). Large horizontal misalignment may result in the change of MI in the dynamic WPT system. The change of MI

Manuscript received September 1, 2023; revised December 20, 2023; accepted May 7, 2024. Date of publication June 30, 2024; date of current version May 17, 2024. This work was supported by National Program on Key Research Project under the grant 2022YFB3403200 and Natural Science Foundation of Hunan Province under the grant 2022JJ30226. *(Corresponding author: Minsheng Yang.)*

Z. Li and S. Huang are with the College of Electrical and Information Engineering, Hunan University, Changsha 410082, China (e-mail: my3eee@126.com; hsd1962@hnu.edu.cn).

Z. Chen, Y. Cheng, and X. Xiong are with the College of Traffic Engineering, Hunan University of Technology, Zhuzhou 412007, China (e-mail: 1105886866@qq.com; Chengyu9810@163.com; hut xxb@163.com).

M. Yang is with the College of Electrical Engineering Hunan University of Arts and Sciences, Changde 415000, China (e-mail: 20253816@qq.com).

Digital Object Identifier 10.24295/CPSSTPEA.2024.00006

may lead to fluctuation in system performance, including the efficiency and output power.

At present, the main methods for solving the effect of horizontal misalignment on output power and efficiency fluctuation are impedance matching methods and coil structure design methods. Impedance matching methods including LC, T, π, LCC-LCC [11], [12], LCL and CL [13], LCC-C [14], LCC-S [15], and DC-DC converters [16] are proposed by scholars. These impedance-matching networks can improve the system performance. However, it is difficult to further improve the performance of WPT systems with large misalignment because the change of MI in the dynamic WPT systems is too fast and large.

The method of designing coil structure may be an effective method to deal with the rapid and large variation in MI. Two types of coil structures are commonly used. The first type is the long-track coil structures; the second type is the short-individual coil structures. Several long-track coil structures, such as E-core structure, U-core structure, W-core structure, S-core structure [17], and I-core structure [18], are proposed successively to keep the MI constant. These structures have good misalignment tolerance. However, the MI of the long-track coil structures is very small. Thus, the short-individual coil structures are proposed to increase the MI. A structure of DD coil is proposed to enhance the MI. This structure has good misalignment in the *Y*-axis. However, the MI in the *X*-axis is highly variable [19]. Therefore, it is recommended to overlap a single-pole (Q) coil and a double-pole (DD) coil to form a DDQ coil to improve the misalignment capability in the *X*-axis [20]. Then, an asymmetric coil structure is proposed. Experiments show that the MI is constant when the misalignment along *Y*-axis or *X*-axis direction are within 10 cm [21]. However, the efficiency of this structure is only 65.6% because of the small MI. An asymmetrical three-coil structure is proposed to improve efficiency and keep the MI constant. However, the maximum misalignment along the *Y*-axis or *X*-axis direction is only 10 cm with this structure [22]. To improve the misalignment distance, a structure with one transmit coil and four cascaded receive coils is proposed. The maximum misalignment along the *Y*-axis direction can reach 24 cm and the fluctuation in MI is 8.4%. However, the MI value of this structure is reduced by 42.79% compared with the traditional structure [23]. To further reduce the reduction rate of MI and the ratio of fluctuation in MI, a reverse series coil is added to the transmitting coil [24]. The fluctuation in MI is 6.4% when the misalignment reaches 50% of the diameter of the transmitting coil. Moreover, a structure of unsymmetrical and the opposite series coil is proposed. The ratio of fluctuation in MI is 4.2% when the misalignment is within 50% of the side length of the transmitting coil [25]. However, compared with the traditional structure, the MI value of this structure is reduced by 32.81%. In summary, the problem of obtaining constant MI at the expense of MI values has not been solved.

In this paper, an edge-enhanced coil (EEC) structure is proposed. By using the EEC structure, not only the MI fluctuation is reduced, but also the MI value is increased. Therefore, higher efficiency and smaller output power fluctuation are also achieved by the proposed structure compared to the traditional structure. Experimental results verify the effectiveness of the EEC structure.

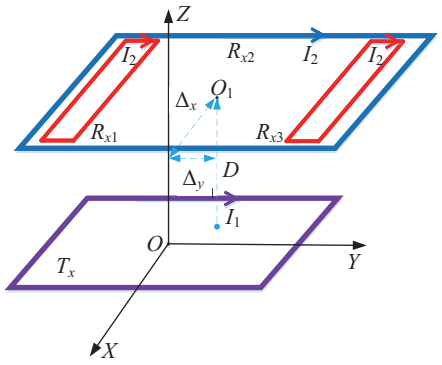

Fig. 2. Schematic of EEC structure. The current of R_{x1} and the current of R_{x2} are the same as the current of R_{x3} in the direction.

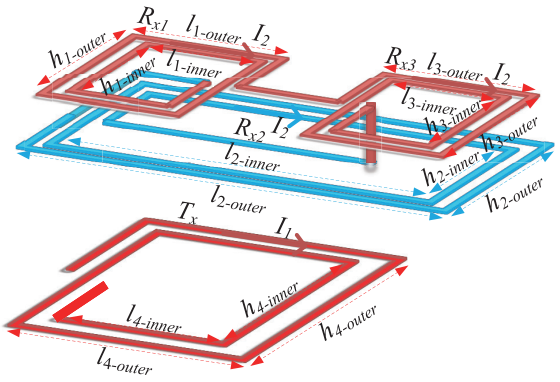

Fig. 3. Dimension drawing of EEC structure.

II. Edge-Enhanced Coil Structure

A. EEC Structure

An edge-enhanced coil (EEC) structure is proposed, as shown in Fig. 2. The EEC structure consists of a transmitting coil and a receiving coil. The transmitting coil is labeled T_x, the receiving coil is labeled R_x. The receiving coil is composed of R_{x1}, R_{x2}, and R_{x3}. The MI at the receiving resonance coil edge can be increased by adding R_{x1} and R_{x3} into R_{x2} when the receiving resonance coil is moved in the *Y*-axis. Parameters Δ_x and Δ_y are the misalignment along the *X*-axis and *Y*-axis, respectively. Parameters I_1 and I_2 are the currents of T_x and R_x, respectively. D is the transmitting distance between T_x and R_x.

Fig. 3 shows the proposed R_x and T_x. Parameters $l_{1-\text{inner}}$, $l_{2-\text{inner}}$, $l_{3-\text{inner}}$ and $l_{4-\text{inner}}$ are the inner length of R_{x1}, R_{x2}, R_{x3}, and T_x, respectively. Parameters $l_{1-\text{outer}}$, $l_{2-\text{outer}}$, $l_{3-\text{outer}}$ and $l_{4-\text{outer}}$ are the outer length of R_{x1}, R_{x2}, R_{x3} and T_x, respectively. Parameters $h_{1-\text{inner}}$, $h_{2-\text{inner}}$, $h_{3-\text{inner}}$ and $h_{4-\text{inner}}$ are the inner width of R_{x1}, R_{x2}, R_{x3}, and T_x, respectively. Parameters $h_{1-\text{outer}}$, $h_{2-\text{outer}}$, $h_{3-\text{outer}}$ and $h_{4-\text{outer}}$ are the outer width of R_{x1}, R_{x2}, R_{x3} and T_x, respectively.

There are two outstanding characteristics of the EEC structure. First, the size of T_x is smaller than that of R_x. The purpose

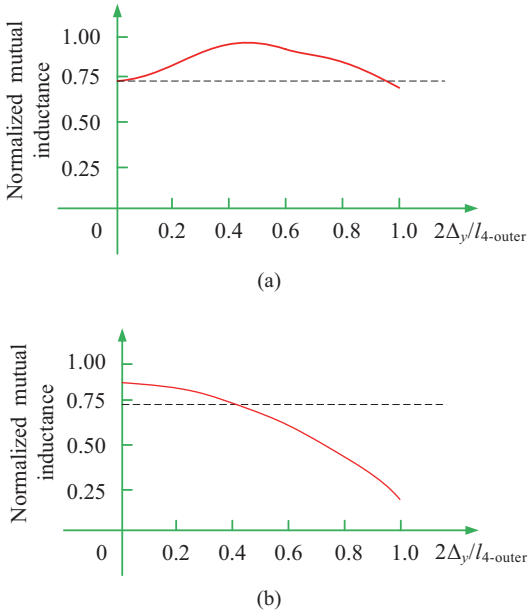

Fig. 4. Normalized mutual inductance versus $2\Delta_y/l_{4\text{-outer}}$. (a) Normalized mutual inductance versus $2\Delta_y/l_{4\text{-outer}}$ with the proposed structure. (b) Normalized mutual inductance versus $2\Delta_y/l_{4\text{-outer}}$ with the traditional structure.

of this design is to reduce MI fluctuation when R_x is moved in the *Y*-axis and *X*-axis directions. Second, R_x is composed of R_{x1}, R_{x2} and R_{x3}. The size of R_{x2} is larger than that of R_{x1} and R_{x3}, R_{x1} is the same as R_{x3} in size. R_{x1} and R_{x3} are on the left and right of R_{x2}, respectively. R_{x1} and R_{x3} are connected to R_{x2} in series in the same direction. The purpose of this design is to increase the magnetic flux density on both sides of R_{x2} in the *Y*-axis direction with the misalignment along the *Y*-axis. Therefore, not only can the MI be increased, but the MI volatility can also be reduced.

When R_x is moved in the *Y*-axis direction, the MI between T_x and R_{x2} may be decreased with the increase of misalignment distance. This phenomenon is consistent with the law of MI of the traditional coil structure. However, in the EEC structure, R_{x1} and R_{x3} are added into R_x. The MI between T_x and R_{x1} may be sharply increased and the MI between T_x and R_{x3} may be slightly decreased. The decrease in MI between T_x and R_{x2} and MI between T_x and R_{x3} are nearly the same as the increase in the MI between T_x and R_{x1}. Therefore, the MI between T_x and R_x can be maintained at a constant. Meanwhile, the MI of the EEC structure is larger than that of the traditional coil structure. This is because the total MI with the EEC structure is equal to the sum of the MI between T_x and R_{x1}, the MI between T_x and R_{x2}, and the MI between T_x and R_{x3}; whereas the total MI with the traditional structure is equal to the MI between T_x and R_{x2} only.

B. Law of MI of EEC Structure

The MI between T_x and R_x of the EEC structure can be obtained as follows:

$$M_{Tx-Rx} = M_{Tx-Rx1} + M_{Tx-Rx2} + M_{Tx-Rx3} \quad (1)$$

where M_{Tx-Rx} is the MI between T_x and R_x, M_{Tx-Rx1} is the MI between T_x and R_{x1}, M_{Tx-Rx2} is the MI between T_x and R_{x2}, M_{Tx-Rx3} is the MI between T_x and R_{x3}.

M_{Tx-Rx} may be maintained constant when the change value of M_{Tx-Rx1} equals the change value of the sum of M_{Tx-Rx2} and M_{Tx-Rx3}. The value of M_{Tx-Rx1} may be increased and the value of M_{Tx-Rx2} and M_{Tx-Rx3} may be decreased with different misalignment along the *Y*-axis direction owing to the two outstanding characteristics in the EEC structure.

Fig. 4(a) shows that M_{Tx-Rx} is not decreased monotonically as Δ_y is increased. Fig. 4(a) shows that M_{Tx-Rx} may be increased when Δ_y is increased. This is because the increase in M_{Tx-Rx1} is larger than that of the decrease in the sum of M_{Tx-Rx2} and M_{Tx-Rx3}. However, M_{Tx-Rx} in the traditional structure is reduced as the misalignment is increased, as shown in Fig. 4(b).

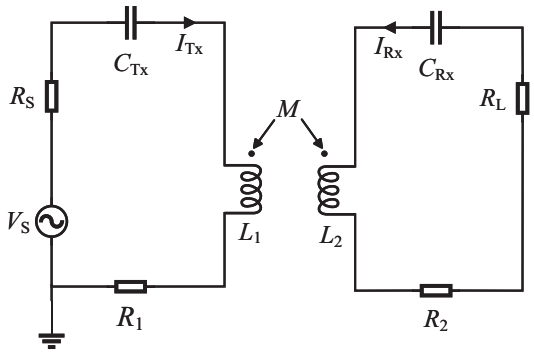

Fig. 5. EEC structure with S-S topology.

C. S-S Topology in EEC Structure

The equivalent circuit model is obtained from the EEC coil structure as shown in Fig. 5. Parameters L_1, L_2, R_1, and R_2 are the self-inductance and internal resistance of the transmitting and receiving coils, respectively. C_{Tx} and C_{Rx} are defined as the resonant capacitance of the transmitting and receiving coils. M is the mutual inductance between the coils and R_S is the internal resistance of the power supply V_S. According to Fig. 5 the matrix of Kirchhoff's voltage equation is obtained as

$$\begin{bmatrix} Z_1 & j\omega M \\ j\omega M & Z_2 \end{bmatrix} \begin{bmatrix} I_{Tx} \\ I_{Rx} \end{bmatrix} = \begin{bmatrix} V_S \\ 0 \end{bmatrix} \quad (2)$$

The currents in the transmitting and receiving coils are given

$$\begin{cases} I_{Tx} = \dfrac{Z_2 V_S}{Z_1 Z_2 + (\omega M)^2} \\ I_{Rx} = -\dfrac{j\omega M V_S}{Z_1 Z_2 + (\omega M)^2} \end{cases} \quad (3)$$

The transmitting coil impedance Z_1 and receiving coil impedance Z_2 are expressed as follows:

$$\begin{cases} Z_1 = R_S + R_1 + j\omega L_1 - j\dfrac{1}{\omega C_{Tx}} \\ Z_2 = R_2 + R_L + j\omega L_2 - j\dfrac{1}{\omega C_{Rx}} \end{cases} \quad (4)$$

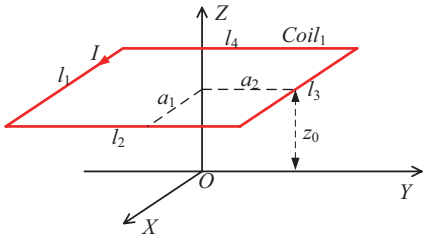

Fig. 6. A single rectangular coil.

According to (3) and (4) the input power P_{in}, output power P_{out} and transmission efficiency η of the system can be obtained

$$P_{in} = V_S I_{Tx} = \left| \frac{Z_2 {V_S}^2}{Z_1 Z_2 + \omega^2 M^2} \right| \tag{5}$$

$$P_{out} = I_{Rx}^2 R_L = \left| - \frac{{V_S}^2 (\omega M)^2 R_L}{(Z_1 Z_2 + \omega^2 M^2)^2} \right| \tag{6}$$

$$\eta = \left| \frac{P_{out}}{P_{in}} \right| = \left| - \frac{(\omega M)^2 R_L}{Z_1 Z_2^2 + (\omega M)^2 Z_2} \right| \tag{7}$$

III. Calculation and Optimization Method of Coupling Coefficient

In this section, a calculation method for the mutual inductance and self-inductance of the rectangular coil is presented to calculate the coupling coefficient of the proposed structure fast. The coupling coefficient is defined as follows:

$$k_{12} = \frac{M_{12}}{\sqrt{L_1 L_2}} \tag{8}$$

where k_{12} is the mutual inductance between two coils, M_{12} is the mutual inductance between two coils, L_1 and L_2 are the self-inductance of two coils.

A. Self-Inductance Calculation of the Rectangular Coil

A schematic diagram of a single-turn rectangular coil is shown in Fig. 6. The half-length and half-width of the rectangular coil are a_1 and a_2, respectively. z_0 is the height of the rectangular coil. $Coil_1$ is separated into four parts (l_1, l_2, l_3, and l_4). The parameter I is the current of the $Coil_1$.

For a current-carrying conductor with a current density J in air, the magnetic vector of any point $P(x, y, z)$ is as follows:

$$A(x, y, z) = \frac{\mu_0}{4\pi} \int_v \frac{J(x', y', z') dv'}{R} \tag{9}$$

where J is the current density and v is the current distribution of $Coil_1$. R is the distance from $P(x, y, z)$ to the source point (x', y', z').

$$R = \sqrt{(x - x')^2 + (y - y')^2 + (z - z')^2} \tag{10}$$

The dual Fourier transformation and its inverse transformation are used to solve (9) [26].

$$b(\xi, \eta, z) = \int_{-\infty}^{\infty} \int_{-\infty}^{\infty} B(x, y, z) e^{-j(x\xi + y\eta)} dx dy \tag{11}$$

$$B(x, y, z) = \frac{1}{4\pi^2} \int_{-\infty}^{\infty} \int_{-\infty}^{\infty} b(\xi, \eta, z) e^{j(x\xi + y\eta)} d\xi d\eta \tag{12}$$

where ξ and η are the double Fourier integral variables.

Substituting (9) into (11), (13) can be obtained as follows:

$$a(\xi, \eta, z) = \frac{\mu_0}{2} \int_v \frac{1}{k} e^{-j(x'\xi + y'\eta)} J(x', y', z') e^{-k|z - z'|} dv' \tag{13}$$

The relationship between the incident magnetic flux density and the magnetic vector potential is as follows:

$$B = \nabla \times A \tag{14}$$

Substituting the Fourier transform into (14), (15) is obtained as follows:

$$\begin{cases} b_x = -j\eta a_z - \dfrac{\partial a_y}{\partial z} \\ b_y = \dfrac{\partial a_x}{\partial z} + j\xi a_z \\ b_z = -j\xi a_y + j\eta a_x \end{cases} \tag{15}$$

where

$$k = \sqrt{\xi^2 + \eta^2} \tag{16}$$

The wires l_1 and l_3 are parallel to the X-axis, and the wires l_2 and l_4 are parallel to the Y-axis. Therefore, the component a_x of the magnetic vector potential in the X-axis direction is generated only by the wires l_1 and l_3. According to (13), the expression of a_x is as follows:

$$\begin{aligned} a_x &= a_{x1} - a_{x3} \\ &= \frac{\mu_0 I e^{ja_2\eta} e^{-|z - z_0|k}}{2k} \left(\int_{-a_1}^{a_1} e^{-jx'\xi} dx' - \int_{-a_1}^{a_1} e^{-jx'\xi} dx' \right) \\ &= \frac{j2\mu_0 I \sin(\xi a_1) \sin(\eta a_2) e^{-|z - z_0|k}}{\xi k} \end{aligned} \tag{17}$$

where a_{x1} and a_{x3} represent the magnetic vector potential components, which are generated by wires l_1 and l_3, respectively.

Similarly, the component of the magnetic vector potential a_y in the Y-axis direction is obtained as follows:

$$a_y = \frac{-j2\mu_0 I \sin(\eta a_2) \sin(\xi a_1) e^{-|z - z_0|k}}{\eta k} \tag{18}$$

Substituting (17) and (18) into (16), (19)-(21) can be obtained as follows:

$$b_x = \frac{\mathrm{j}2\mu_0 I \sin(\xi a_1)\sin(\eta a_2)}{\eta} \tag{19}$$

$$b_y = \frac{\mathrm{j}2\mu_0 I \sin(\xi a_2)\sin(\eta a_1)}{\xi} \tag{20}$$

$$b_z = \frac{-2\mu_0 Ik \sin(\xi a_1)\sin(\eta a_2)}{\xi\eta} \tag{21}$$

Substituting (19), (20), and (21) into (12), the magnetic flux density in the $z = z_0$ plane is obtained.

$$B_x = \int_{-\infty}^{\infty}\int_{-\infty}^{\infty} \frac{\mathrm{j}2\mu_0 I \sin(\xi a_1)\sin(\eta a_2)}{4\pi^2\eta} \mathrm{e}^{\mathrm{j}(x\xi+y\eta)}\mathrm{d}\xi\mathrm{d}\eta \tag{22}$$

$$B_y = \int_{-\infty}^{\infty}\int_{-\infty}^{\infty} \frac{\mathrm{j}2\mu_0 I \sin(\xi a_2)\sin(\eta a_1)}{4\pi^2\xi} \mathrm{e}^{\mathrm{j}(x\xi+y\eta)}\mathrm{d}\xi\mathrm{d}\eta \tag{23}$$

$$B_z = \int_{-\infty}^{\infty}\int_{-\infty}^{\infty} \frac{-2\mu_0 Ik \sin(\xi a_1)\sin(\eta a_2)}{4\pi^2\xi\eta} \mathrm{e}^{\mathrm{j}(x\xi+y\eta)}\mathrm{d}\xi\mathrm{d}\eta \tag{24}$$

For a single rectangular coil, only the magnetic flux density in the *Z*-axis direction needs to be considered when the self-inductance is calculated. According to (24), the self-inductance calculation formula of a single rectangular coil is obtained as follows:

$$L = \frac{1}{I}\oint\!\!\oint B_z \mathrm{d}s = \int_{-\infty}^{\infty}\int_{-\infty}^{\infty}\int_{-a_1}^{a_1}\int_{-a_2}^{a_2} \frac{-2\mu_0 k \sin(\xi a_1)\sin(\eta a_2)}{4\pi^2\xi\eta} \mathrm{e}^{\mathrm{j}(x\xi+y\eta)}\mathrm{d}y\mathrm{d}x\mathrm{d}\xi\mathrm{d}\eta \tag{25}$$

B. Mutual Inductance Calculation Method of the Rectangular Coil

A method for calculating the mutual inductance of rectangular coils based on the vector potential is proposed. A schematic diagram of two rectangular coils, $Coil_1$ and $Coil_2$, is shown in Fig. 7. a_1 and a_2 are the half-length and half-width of $Coil_1$. b_1 and b_2 are the half-length and half-width of $Coil_2$. $Coil_1$ is separated into four parts (l_1, l_2, l_3, and l_4). z_0 is the vertical distance between o and o_1, and z_1 is the vertical distance between o and o_2. The parameter I is the current of $Coil_1$.

It is noted that $z \neq z_0$ when the mutual inductance between T_x and R_x is calculated. By substituting (17) and (18) into (15), the following is obtained:

$$b_{ix} = C_{ix} \cdot \mathrm{e}^{-kz} \tag{26}$$

$$b_{iy} = C_{iy} \cdot \mathrm{e}^{-kz} \tag{27}$$

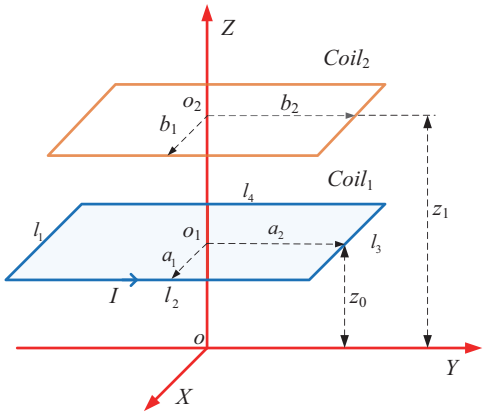

Fig. 7. Schematic diagram of two rectangular coils.

$$b_{iz} = C_{iz} \cdot \mathrm{e}^{-kz} \tag{28}$$

where

$$C_{ix} = \frac{-\mathrm{j}2\mu_0 I \sin(\xi a_1)\sin(\eta a_2)}{\eta} \mathrm{e}^{z_0 k} \tag{29}$$

$$C_{iy} = \frac{-\mathrm{j}2\mu_0 I \sin(\xi a_1)\sin(\eta a_2)}{\xi} \mathrm{e}^{z_0 k} \tag{30}$$

$$C_{iz} = \frac{-2\mu_0 Ik \sin(\xi a_1)\sin(\eta a_2)}{\xi\eta} \mathrm{e}^{z_0 k} \tag{31}$$

By substituting (26), (27), and (28) into (12), the magnetic flux density B_i is obtained as follows:

$$B_{ix}(x,y,z) = \frac{1}{4\pi^2}\int_{-\infty}^{\infty}\int_{-\infty}^{\infty} C_{ix} \cdot \mathrm{e}^{-kz} \cdot \mathrm{e}^{\mathrm{j}(x\xi+y\eta)}\mathrm{d}\xi\mathrm{d}\eta \tag{32}$$

$$B_{iy}(x,y,z) = \frac{1}{4\pi^2}\int_{-\infty}^{\infty}\int_{-\infty}^{\infty} C_{iy} \cdot \mathrm{e}^{-kz} \cdot \mathrm{e}^{\mathrm{j}(x\xi+y\eta)}\mathrm{d}\xi\mathrm{d}\eta \tag{33}$$

$$B_{iz}(x,y,z) = \frac{1}{4\pi^2}\int_{-\infty}^{\infty}\int_{-\infty}^{\infty} C_{iz} \cdot \mathrm{e}^{-kz} \cdot \mathrm{e}^{\mathrm{j}(x\xi+y\eta)}\mathrm{d}\xi\mathrm{d}\eta \tag{34}$$

According to (32), (33), and (34), the mutual inductance between $Coil_1$ and $Coil_2$ can be obtained

$$M_{12} = \oint\!\!\oint_{\mathrm{D}} \frac{B}{I} \cdot \mathrm{d}s = \int_{-\infty}^{\infty}\int_{-\infty}^{\infty} \frac{(C_{iz}+C_{ix})}{4\pi^2 I} \cdot \frac{\mathrm{e}^{\mathrm{j}(b_{1d}+b_1)\xi} - \mathrm{e}^{\mathrm{j}(b_{1d}-b_1)\xi}}{\mathrm{j}\xi} \cdot \frac{\mathrm{e}^{\mathrm{j}(b_{2d}+b_2)\eta} - \mathrm{e}^{\mathrm{j}(b_{2d}-b_2)\eta}}{\mathrm{j}\eta} \cdot \mathrm{e}^{-ks_2}\mathrm{d}\xi\mathrm{d}\eta \tag{35}$$

where b_{1d} and b_{2d} are the misalignment of the *X*-axis and *Y*-axis, respectively.

The mutual inductance between multi-turn coils is calculated as follows:

$$M = \sum_{m=1}^{N_1} \sum_{n=1}^{N_2} M_{\mathrm{mn}} \tag{36}$$

where N_1 is the number of turns of $Coil_1$, N_2 is the number of turns of $Coil_2$, m is the m-th turn of $Coil_1$, and n is the n-th turn of $Coil_2$.

The calculation method of the coupling coefficient provides the theoretical basis for analyzing and optimizing the coupling coefficient of the proposed structure in the next subsection.

C. Optimization Method of Parameters of EEC Structure

In the previous section, it is theoretically analyzed that the MI fluctuation rate may be reduced and the MI value may be increased by using the EEC structure at the same time. In this section, an optimization method of parameters of the EEC structure is proposed to obtain the quasi-constant MI when Δ_y and Δ_x are within 50% of the side length of T_x and 10 cm, respectively. The optimization process is as follows:

1) Parameters initialization: D is set to 15 cm. The copper wire diameter is set to 0.25 cm. Parameters ε_{1_Y} and ε_{2_Y} are the fluctuations in MI when Δ_y is within 50% of the side length of the transmitting coil. ε_{1_X} and ε_{2_X} are the fluctuations in MI when Δ_x is within 10 cm. $\varepsilon_{1\_Y^*}$, $\varepsilon_{2\_Y^*}$, $\varepsilon_{1\_X^*}$, and $\varepsilon_{2\_X^*}$ are set to 5%. $M_{Tx-Rx-0^*}$ is set to 25 μH. The coupling coefficient between T_x and R_x ($k_{Tx-Rx-0^*}$) is set to 0.11. All rates of fluctuation in MI along the *Y*-axis and *X*-axis are defined as

$$\varepsilon_{1\_Y} = (M_{Tx-Rx-\max\_Y} - M_{Tx-Rx-0})/M_{Tx-Rx-0} \tag{37}$$

$$\varepsilon_{2\_Y} = |(M_{Tx-Rx-\min\_Y} - M_{Tx-Rx-0})/M_{Tx-Rx-0}| \tag{38}$$

$$\varepsilon_{1\_X} = (M_{Tx-Rx-\max\_X} - M_{Tx-Rx-0})/M_{Tx-Rx-0} \tag{39}$$

$$\varepsilon_{2\_X} = |(M_{Tx-Rx-\min\_X} - M_{Tx-Rx-0})/M_{Tx-Rx-0}| \tag{40}$$

where $M_{Tx-Rx-0}$ is the MI between T_x and R_x with Δ_x= 0 cm and Δ_y = 0 cm. $M_{Tx-Rx-\max\_Y}$ and $M_{Tx-Rx-\min\_Y}$ are the maximum and minimum MI between T_x and R_x with misalignment along the *Y*-axis, respectively. $M_{Tx-Rx-\max\_X}$ and $M_{Tx-Rx-\min\_X}$ are the maximum and minimum MI between T_x and R_x with misalignment along the *X*-axis, respectively.

2) Constraint conditions setting: Constraint conditions of each coil parameter are as follows: 21 cm $\leqslant l_{1-\mathrm{inner}} \leqslant$ 23 cm, 54 cm $\leqslant l_{2-\mathrm{inner}} \leqslant$ 56 cm, 21 cm $\leqslant l_{3-\mathrm{inner}} \leqslant$ 23 cm, 26 cm $\leqslant l_{4-\mathrm{inner}} \leqslant$ 27 cm, 57 cm $\leqslant h_{1-\mathrm{inner}} \leqslant$ 58 cm, 54 cm $\leqslant h_{2-\mathrm{inner}} \leqslant$ 56 cm, 57 cm $\leqslant h_{3-\mathrm{inner}} \leqslant$ 58 cm, 26 cm $\leqslant h_{4-\mathrm{inner}} \leqslant$ 27 cm. The parameters of R_{x1} and R_{x3} are set to be the same. N_1 and N_2 are the numbers of turns for T_x and R_{x2}, respectively. N_3 is the number of turns for R_{x1} and R_{x3}. N_1 is changed from 16 turns to 20 turns. N_2 is changed from 9 turns to 13 turns. N_3 is changed from 3 turns to 7 turns. The step of the number of turns is 1 turn. The variation of both the length and width is 1 cm.

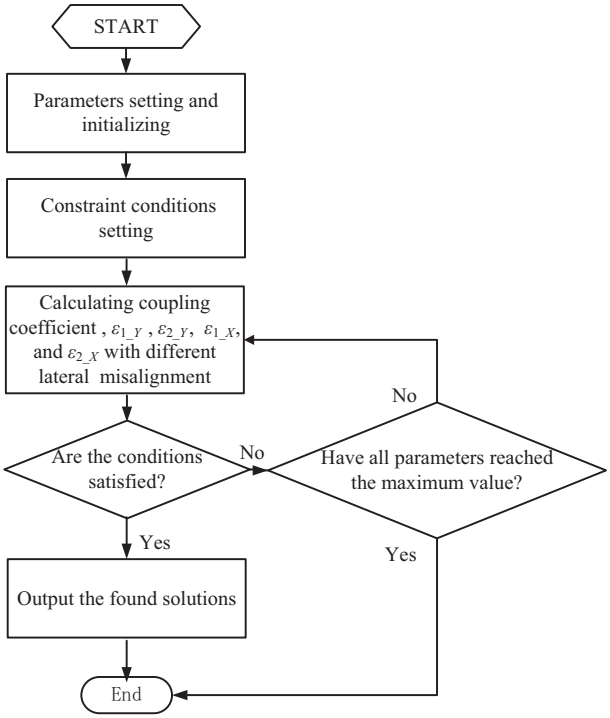

Fig. 8. Flowchart of the optimization method of the mutual inductance.

3) Calculation: The MI with the EEC structure can be calculated according to (35) and (36) with different misalignment along the *Y*-axis, and *X*-axis. ε_{1_Y} and ε_{2_Y} can be calculated by (37) and (38). ε_{1_X} and ε_{2_X} can be calculated by (39) and (40).

4) Conditional judgment and output solutions: Two conditions should be met at the same time. ① $\varepsilon_{1\_Y} < \varepsilon_{1\_Y^*}$, $\varepsilon_{2\_Y} < \varepsilon_{2\_Y^*}$, $\varepsilon_{1\_X} < \varepsilon_{1\_X^*}$, and $\varepsilon_{2\_X} < \varepsilon_{2\_X^*}$. ② $M_{Tx-Rx-0} > M_{Tx-Rx-0^*}$ and $k_{Tx-Rx-0} > k_{Tx-Rx-0^*}$. Solutions that meet the above two conditions are output. The flowchart of the proposed method is shown in Fig. 8.

IV. Verification

The experimental setup and simulation model are built based on the EEC structure. The measurement of the MI is obtained. Measurement results agree with calculation results and simulation results. The experimental results show that the MI value of the EEC coil structure increases and then decreases when Δ_y is within 50% of the side length of the transmitting coil, and the fluctuation rate is almost constant.

A. Experimental and Simulation Setup

The simulation model of the EEC structure is established by using Ansys Maxwell, as shown in Fig. 9. Simulation results of the MI can be obtained.

According to the optimization results in the previous section, the dimensions of each coil can be obtained as shown in Table I. The diameter of the Litz wire is 0.25 mm. Measurement parameters of T_x and R_x are shown in Table II.

In addition, an experimental setup is established, including a power source, T_x, R_x, and load, as shown in Fig. 10(a). The

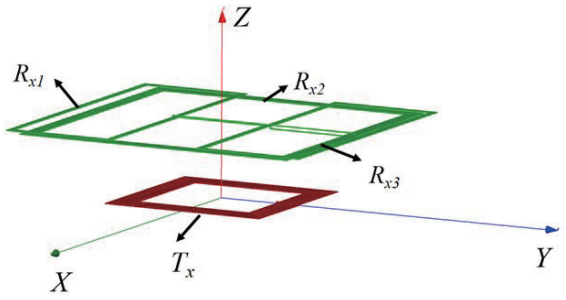

Fig. 9. Simulation model.

TABLE I
DIMENSIONS OF EACH COIL IN THE EXPERIMENT AND SIMULATION

Coil	Dimension of each coil				
	Inner Length (cm)	Inner Width (cm)	Outer Length (cm)	Outer Width (cm)	Number of turns
T_x	26.0	26.0	34.0	34.0	17
R_{x1}	23.0	57.0	26.0	60.0	7
R_{x2}	54.0	54.0	60.0	60.0	13
R_{x3}	23.0	57.0	26.0	60.0	7

TABLE II
MEASURED PARAMETERS OF THE RESONANCE COILS WITH THE PROPOSED STRUCTURE

Symbol	Quantity	Value
L_{Tx}	the inductance of T_x	186.412 μH
L_{Rx}	the inductance of R_x	580.893 μH
C_1	compensation capacitance of T_x	18.807 nF
C_2	compensation capacitance of R_x	6.035 nF
R_1	the parasitic resistor of T_x	0.253 Ω
R_2	the parasitic resistor of R_x	0.640 Ω
f_0	the original resonance frequency	85.000 kHz

transmitting coil is shown in Fig. 10(b) and the receiving coil is shown in Fig. 10(c).

B. Mutual Inductance Results

As described in reference [26], [27], the MI calculation results can be obtained by using MATLAB. The simulation results of MI are obtained by using Ansys Maxwell model. The measurement results of the MI are obtained by using an IM3536 precision LCR meter.

The MI of the EEC structure versus Δ_y is shown in Fig. 11(a). The MI is almost constant at 35000 μH. For different Δ_y, the MI and the rates of variation of the MI are shown in Table III. As shown in Table III, the maximum MI is 35.625 μH at Δ_y = 8.5 cm, the minimum MI is 33.260 μH at Δ_y = 17.0 cm, and the MI is 34.925 μH at Δ_y = 0 cm. According to (37) and (38), the rates of variation in the MI ε_{1_Y} and ε_{2_Y} are 2.00% and 4.77%, respectively, with different Δ_y.

The MI of the EEC structure versus Δ_x is shown in Fig. 11(b). The MI is also nearly constant at 35.000 μH. The MI and the rates of fluctuation in MI are shown in Table IV with Δ_x. As

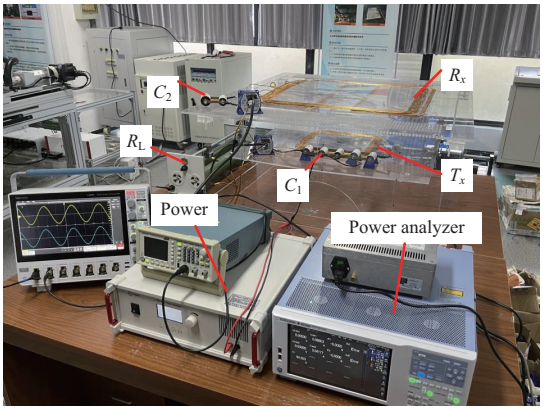

(a)

(b)

(c)

Fig. 10. Experimental setup. (a) Setup. (b) T_x. (c) R_x.

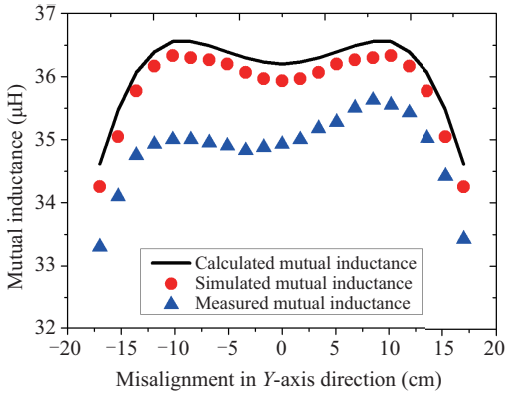

(a)

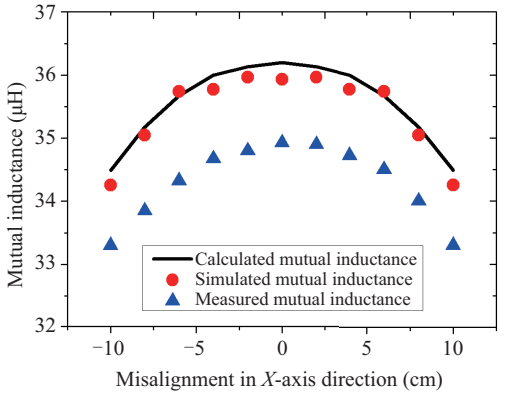

(b)

Fig. 11. Mutual inductance of the proposed structure versus misalignment. (a) Mutual inductance versus misalignment along the *Y*-axis. (b) Mutual inductance versus misalignment along the *X*-axis.

TABLE III
ε_{1_X}, ε_{2_X}, AND MI WITH MISALIGNMENT ALONG THE *X*-AXIS

Mode	$M_{Tx-Rx-0}$	$M_{Tx-Rx-\max\_X}$	$M_{Tx-Rx-\min\_X}$	ε_{1_X}	ε_{2_X}
Calculation values	36.197	36.197	34.486	0.00%	4.73%
Simulation values	35.934	35.934	34.256	0.00%	4.67%
Measurement values	34.925	34.925	33.250	0.00%	4.80%

TABLE IV
ε_{1_y}, ε_{2_y}, AND MI WITH MISALIGNMENT ALONG THE *Y*-AXIS

Mode	$M_{Tx-Rx-0}$	$M_{Tx-Rx-\max\_Y}$	$M_{Tx-Rx-\min\_Y}$	ε_{1_Y}	ε_{2_Y}
Calculation values	36.197	36.559	34.618	1.00%	4.36%
Simulation values	35.934	36.296	34.256	1.01%	4.67%
Measurement values	34.925	35.625	33.260	2.00%	4.77%

shown in Table IV, the maximal MI is 34.925 μH with Δ_x= 0.0 cm and the minimal MI is 33.250 μH with Δ_x=10.0 cm. According to (39) and (40), the rates of fluctuation in MI ε_{1_X} and ε_{2_X} are equal to 0.00% and 4.80% with the misalignment along the *X*-axis, respectively.

The research results show that the fluctuation of MI is less than 5.0% for both the misalignment along the *Y*-axis and *X*-axis directions, which meets the design requirements.

C. Efficiency and Output Power

Parameter Δ_y is changed from 0 cm to 17 cm with a step of 1.7 cm. And Parameter Δ_x is changed from 0 cm to 10 cm with a step of 2 cm. Parameter D is set at 15 cm. The model of the power amplifier is Aigtek ATA-3090, The gain of the power amplifier is set to 15. The load resistor (R_L) is set at 42.0 Ω. The input voltage of T_x (U_1), the input current of T_x (I_1), the output voltage of R_x (U_2), and the output current of R_x (I_2) of the proposed structure are measured by using a Yokogawa WT5000 Power analyzer. The measuring schematic diagram of the output power (P_{out}) and transmission efficiency (η) is shown in Fig. 12.

When the misalignment along the *Y*-axis (Δ_y) is within 17.0 cm, the measured η and P_{out} versus different Δ_y are shown in Fig. 13(a). As can be seen in Fig. 13(a), η is nearly constant with different Δ_y, the maximum efficiency is 95.35% with Δ_y = 8.5 cm, and the minimum efficiency is 94.03% with Δ_y = 17.0 cm. The rate of change in η is only 1.38%. P_{out} is varied from 115.36 W to 119.35 W with Δ_y varying from 0 cm to 6.8 cm. And P_{out} is varied from 118.97 W to 126.74 W with Δ_y varying from 8.5 cm to 17.0 cm. It can be concluded that the variation in P_{out} is 9.86% with the different Δ_y.

When Δ_x is within 10.0 cm, the measured η and P_{out} versus different Δ_x are shown in Fig. 13(b). As can be seen in Fig. 13(b), η is also nearly constant for different Δ_x, the maximum efficiency is 95.35% with Δ_x = 0.0 cm, and the minimum efficiency is

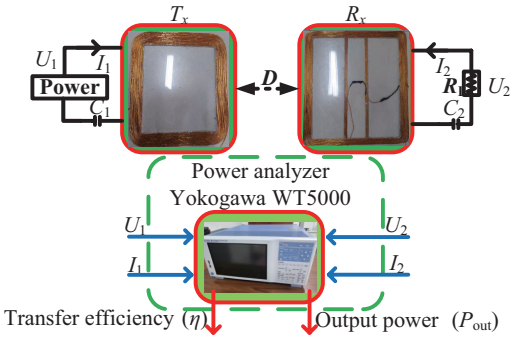

Fig. 12. Schematic diagram of test principle.

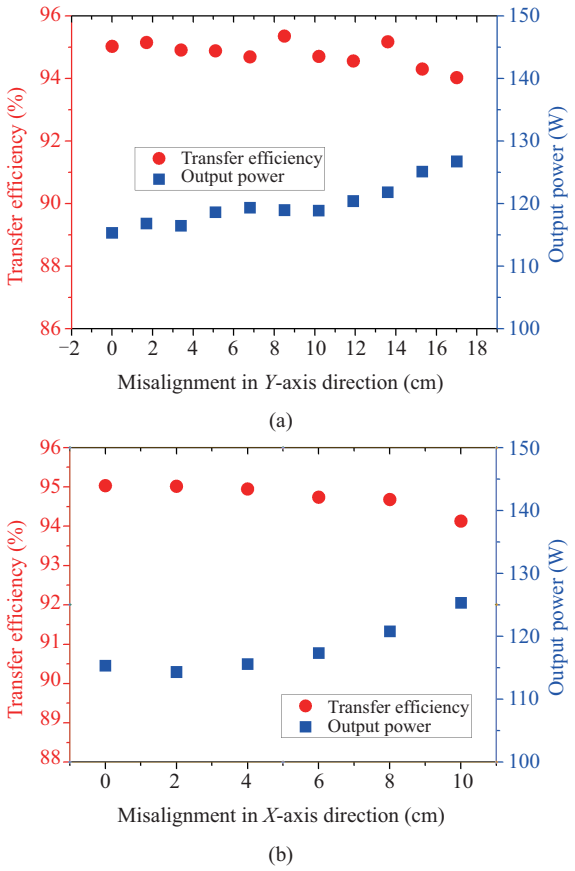

Fig. 13. Transfer efficiency and output power versus misalignment with the proposed structure. (a) Transfer efficiency and output power versus misalignment along the *Y*-axis. (b) Transfer efficiency and output power versus misalignment along the *X*-axis.

94.13% with Δ_x = 10.0 cm. The rate of change in efficiency is 1.27%. P_{out} is varied from 114.32 W to 125.32 W when misalignment along the *X*-axis is within 10.0 cm. The rate of change in P_{out} is 9.62% with misalignment along the *X*-axis. The research results show that the fluctuations of the transfer efficiency and P_{out} are very small. This is due to the fluctuation of MI is small with different misalignments in the proposed structure.

D. Comparison

The conventional structure is composed of T_x and R_{x2} only,

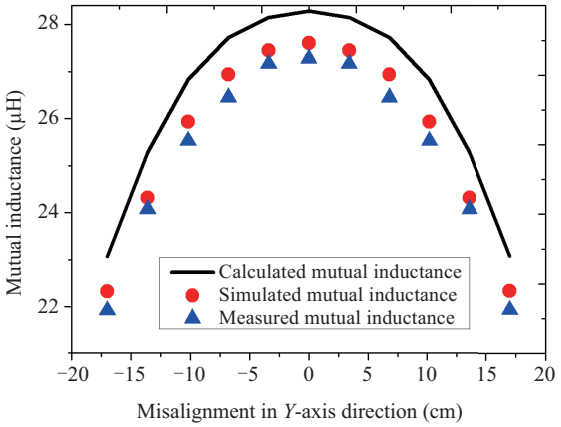

Fig. 14. Mutual inductance of the traditional structure versus misalignment.

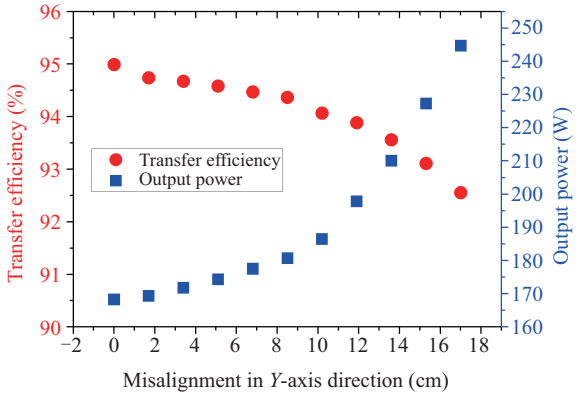

Fig. 15. Transfer efficiency and output power versus misalignment with the traditional structure.

TABLE V
PERFORMANCE COMPARISON

References	Size of T_x (Length*width)	Size of R_x (Length*width)	Misalignment (cm)	Fluctuation in MI (%)	Fluctuation in output power (%)	Fluctuation in efficiency (%)	Maximum efficiency	Is MI increased?
[17]	30 cm*20 cm	100 cm*80 cm	X-direction: 24 Y-direction: /	/	50.0	30.0	74.0	/
[18]	20 cm*10 cm	100 cm*80 cm	X-direction: 30 Y-direction: 15	/	50.0	30.1	71.0	/
[23]	Diameter: 38 cm	Diameter: 60 cm	X-direction: 24 Y-direction: 24	8.4	14.2	2.8	77.2	×
[25]	39 cm*49 cm	65 cm*42 cm	X-direction: / Y-direction: 20	4.2	7.4	1.4	91.0	×
[ourwork]	34 cm*34 cm	65 cm*60 cm	X-direction: 10 Y-direction: 17	4.8	9.9	1.4	95.4	√

where "/" denotes that the value is not given in the reference.

whereas the EEC structure is composed of T_x, R_{x1}, R_{x2}, and R_{x3}. The performance comparison between the conventional structure and the EEC structure is presented. It is found that the MI of the conventional structure is smaller than that of the EEC structure and the fluctuation in MI of the conventional structure is larger than that of the EEC structure. Therefore, the fluctuation in η and P_{out} of the conventional structure are larger than those of the EEC structure. Experimental results further prove the progressiveness of the EEC structure.

The MI of the conventional structure versus different Δ_y is shown in Fig. 14. As shown in Fig. 14, the maximum MI is 27.274 μH with Δ_y = 0.0 cm and the minimum MI is 21.923 μH with Δ_y = 17.0 cm. In addition, ε_{1_Y} and ε_{2_Y} are 0.00% and 19.60%, respectively, when Δ_y is within 17.0 cm. The MI and the rates of fluctuation of the MI with the misalignment along the X axis are the same as those with the misalignment along the Y axis. This is because T_x and R_{x2} are square coil structures.

When Δ_y is within 17.0 cm, the rates of fluctuation in the MI with the conventional structure are much greater than those with the EEC structure. The maximum rate of fluctuation in the MI with the conventional structure is 19.60%, while the maximum rate of fluctuation in the MI with the proposed structure is only 4.80%. Fig. 15 shows η and P_{out} versus misalignment along the Y-axis with the traditional structure. η is varied from 94.99% to 92.55% and P_{out} is varied from 168.23 W to 244.71 W. The rates of fluctuation in P_{out} and η are 45.40% and 2.57%, respectively. The η and P_{out} with the misalignment along the X-axis are the same as those with the misalignment along the Y-axis. This is because T_x and R_{x2} are square coil structures. The P_{out} of the conventional structure is larger than that of the EEC structure because too large MI can lead to power splitting in the proposed structure [25].

The performance comparison between other references and our work is shown in Table V. Compared to the literature [17], [18], [23], and [25], only our proposed structure can reduce the fluctuation in MI and increase the MI value at the same time. Therefore, η is the highest in our work. In addition, the MI can be maintained almost constant in our work when the receiving coil is moved in the Y-axis or X-axis directions simultaneously. Therefore, the proposed structure in our work has two directions of offset capability. The proposed structure can be used to simultaneously satisfy the dynamic and static wireless charging requirements of EVs.

V. CONCLUSION

In this paper, an edge-enhanced coil (EEC) structure is proposed. Moreover, an optimization method of parameters of the EEC structure is proposed to obtain the optimal coil parameters. It is found that the MI of the EEC structure can

not only be kept quasi-constant, but also be increased with misalignment along the *Y*-axis. The problem that quasi-constant MI is obtained at the expense of MI value is solved. The experimental results show that the MI reaches 35.625 μH with $\Delta_y = 8.5$ cm and the MI equals 34.925 μH with $\Delta_y = 0.0$ cm in the EEC structure. The fluctuation in MI is within 4.80%. The transmission efficiency of the EEC structure is also higher due to the increase of MI. And the maximum transmission efficiency is 95.35% when Δ_y and Δ_x are within 50% of the side length of T_x and 10.0 cm, respectively.

It is worth noting that the transfer efficiency and output power can be maintained nearly constant without additional auxiliary control devices, although the maximal Δ_y reaches 50% of the side length of T_x. This will result in significant cost savings and reduce the difficulty of controlling the DSWPT systems. Therefore, the EEC structure can be used to simultaneously satisfy the dynamic and static wireless charging requirements of EVs. In future research, we will study on adding a magnetic medium to the EEC structure to obtain a greater MI and a smaller fluctuation in MI.

References

[1] S. Y. R. Hui, "Past, present and future trends of non-radiative wireless power transfer," in *CPSS Transactions on Power Electronics and Applications*, vol. 1, no. 1, pp. 83–91, Dec. 2016.

[2] C. Liao, J. Li, and S. Li, "Design of LCC impedance matching circuit for wireless power transfer system under rectifier load," in *CPSS Transactions on Power Electronics and Applications*, vol. 2, no. 3, pp. 237–245, Sep. 2017.

[3] E. Abramov, I. Zeltser, and M. M. Peretz, "A network-based approach for modeling resonant capacitive wireless power transfer systems," in *CPSS Transactions on Power Electronics and Applications*, vol. 4, no. 1, pp. 19–29, Mar. 2019.

[4] Y. Zhang, S. Chen, X. Li, and Y. Tang, "Design of high-power static wireless power transfer via magnetic induction: An overview," in *CPSS Transactions on Power Electronics and Applications*, vol. 6, no. 4, pp. 281–297, Dec 2021.

[5] C. Rong, B. Zhang, Y. Jiang, X. Shu, and Z. Wei, "A misalignment-tolerant fractional-order wireless charging system with constant current or voltage output," in *IEEE Transactions on Power Electronics*, vol. 37, no. 9, pp. 11356–11368, Sept. 2022.

[6] Z. Yan, Y. Zhang, T. Kan, F. Lu, K. Zhang, B. Song, and C. C. Mi, "Frequency optimization of a loosely coupled underwater wireless power transfer system considering eddy current loss," in *IEEE Transactions on Industrial Electronics*, vol. 66, no. 5, pp. 3468–3476, May 2019.

[7] Z. Yan, B. Song, Y. Zhang, K. Zhang, Z. Mao, and Y. Hu, "A rotation-free wireless power transfer system with stable output power and efficiency for autonomous underwater vehicles," in *IEEE Transactions on Power Electronics*, vol. 34, no. 5, pp. 4005–4008, May 2019.

[8] Z. Yan, K. Zhang, L. Qiao, Y. Hu, and B. Song, "A multiload wireless power transfer system with concentrated magnetic field for auv cluster system," in *IEEE Transactions on Industry Applications*, vol. 58, no. 1, pp. 1307–1314, Jan.-Feb. 2022

[9] Z. Zhang, S. Shen, Z. Liang, S. H. K. Eder, and R. Kennel, "Dynamic-balancing robust current control for wireless drone-in-flight charging," in *IEEE Transactions on Power Electronics*, vol. 37, no. 3, pp. 3626–3635, Mar. 2022.

[10] Y. Zhang, Y. Wu, W. Pan, H. Wang, Z. Shen, X. Li, X. Mao, and Z. Li, "Free positioning wireless charging system based on tilted long-track transmitting coil array," in *IEEE Transactions on Circuits and Systems II: Express Briefs*, vol. 69, no. 9, pp. 3849–3853, Sept. 2022.

[11] Z. Luo, Y. Zhao, M. Xiong, X. Wei, and H. Dai, "A self-tuning LCC/LCC system based on switch-controlled capacitors for constant-power wireless electric vehicle charging," in *IEEE Transactions on Industrial Electronics*, vol. 70, no. 1, pp. 709–720, Jan. 2023.

[12] M. Mohammad, O. C. Onar, G.-J. Su, J. Pries, V. P. Galigekere, S. Anwar, E. Asa, J. Wilkins, R. Wiles, C. P. White, *et al*, "Bidirectional LCC–LCC-compensated 20-kW wireless power transfer system for medium-duty vehicle charging," in *IEEE Transactions on Transportation Electrification*, vol. 7, no. 3, pp. 1205–1218, Sept. 2021.

[13] Y. Yao, Y. Wang, X. Liu, F. Lin, and D. Xu, "A novel parameter tuning method for a double-sided lcl compensated wpt system with better comprehensive performance," in *IEEE Transactions on Power Electronics*, vol. 33, no. 10, pp. 8525–8536, Oct. 2018.

[14] C. Xiao, D. Cheng, and K. Wei, "An LCC-C compensated wireless charging system for implantable cardiac pacemakers: theory, experiment, and safety evaluation," in *IEEE Transactions on Power Electronics*, vol. 33, no. 6, pp. 4894–4905, Jun. 2018.

[15] Z. Yan, Y. Zhang, K. Zhang, B. Song, S. Li, T. Kan, and C. C. Mi, "Fault-tolerant wireless power transfer system with a dual-coupled LCC-S topology," in *IEEE Transactions on Vehicular Technology*, vol. 68, no. 12, pp. 11838–11846, Dec. 2019.

[16] A. P. Sample, B. H. Waters, S. T. Wisdom, and J. R. Smith, "Enabling seamless wireless power delivery in dynamic environments," in *Proceedings of the IEEE*, vol. 101, no. 6, pp. 1343–1358, Jun. 2013.

[17] S. Y. Choi, S. Y. Jeong, E. S. Lee, B. W. Gu, S. W. Lee, and C. T. Rim, "Generalized models on self-decoupled dual pick-up coils for large lateral tolerance," in *IEEE Transactions on Power Electronics*, vol. 30, no. 11, pp. 6434–6445, Nov. 2015.

[18] J. Huh, S. W. Lee, W. Y. Lee, G. H. Cho, and C. T. Rim, "Narrow-width inductive power transfer system for online electrical vehicles," in *IEEE Transactions on Power Electronics*, vol. 26, no. 12, pp. 3666–3679, Dec. 2011.

[19] S. Y. Choi, B. W. Gu, S. Y. Jeong, and C. T. Rim, "Advances in wireless power transfer systems for roadway-powered electric vehicles," in *IEEE Journal of Emerging and Selected Topics in Power Electronics*, vol. 3, no. 1, pp. 18–36, Mar. 2015.

[20] M. Budhia, J. T. Boys, G. A. Covic, and C.-Y. Huang, "Development of a single-sided flux magnetic coupler for electric vehicle IPT charging systems," in *IEEE Transactions on Industrial Electronics*, vol. 60, no. 1, pp. 318–328, Jan. 2013.

[21] Z. Li, W. Cheng, J. Yi, and J. Li, "Design and optimization of quasi-constant mutual inductance for asymmetric two-coil wireless power transfer system with lateral misalignments," in *Progress In Electromagnetics Research M*, vol. 69, pp. 207–217, Jun. 2018.

[22] Z. Li, M. Zhang, S. Huang, and J. Yi, "Design and optimization of structure of tower-type coil in wireless charging system for electric vehicles," in *Progress In Electromagnetics Research B*, vol. 85, pp. 85–101, Aug. 2019.

[23] Z. Li and J. Yi, "Modeling and design of a transmission coil and four cascaded receiving coils wireless charging structure with lateral misalignments," in *IEEE Access*, vol. 8, pp. 75976–75985, Apr. 2020.

[24] Y. Chen, R. Mai, Y. Zhang, M. Li, and Z. He, "Improving misalignment tolerance for IPT system using a third-coil," in *IEEE Transactions on Power Electronics*, vol. 34, no. 4, pp. 3009–3013, Apr. 2019.

[25] Z. Li, J. Li, S. Li, Y. Yu, and J. Yi, "Design and optimization of asymmetric and reverse series coil structure for obtaining quasi-constant mutual inductance in dynamic wireless charging system for electric vehicles," in *IEEE Transactions on Vehicular Technology*, vol. 71, no. 3, pp. 2560–2572, Mar. 2022.

[26] S. Zhang, J. Tang, and W. Wu, "Calculation model for the induced voltage of pick-up coil excited by rectangular coil above conductive plate," in *2015 IEEE International Conference on Mechatronics and Automation (ICMA)*, Beijing, China, 2015, pp. 1805–1810.

[27] Z. Luo and X. Wei, "Analysis of square and circular planar spiral coils in wireless power transfer system for electric vehicles," in *IEEE Transactions on Industrial Electronics*, vol. 65, no. 1, pp. 331–341, Jan. 2018.

Minsheng Yang graduated from Hunan University with a Ph.D. in 2012, and is currently the Vice Dean of the School of Computer and Electrical Engineering at Hunan University of Arts and Sciences, where he has long been engaged in research and teaching related to the fields of electrical energy conversion and control, electrical control technology, electrical equipment intelligence and intelligent control.

Yu Cheng was born in China in 1998. He received a Bachelor's degree in Mechanical Design-Manufacture and Automation from College of Science and Technology Ningbo University, NingBo, China, in 2021. He is currently pursuing the Master's degree in Electronic Information at Hunan University of Technology. His current research interests include wireless power transfer systems.

Xinbo Xiong was born in China in 1998. He received a Bachelor's degree in Electrical Engineering and Automation from Hohai University, NanJing, China, in 2020. He is currently pursuing the Master's degree in Energy Power at Hunan University of Technology. His current research interests include wireless power transfer systems.

Zhongqi Li was born in China in 1985. He received the M.Sc. degree from Hunan University of Technology, China in 2012, and the Ph.D. degree from the Hunan University in 2016. From 2016, he is working Assistant Professor in Hunan University of Technology, China. From 2020, he is now working postdoctoral fellow in Hunan University. His research interests include wireless power transfer systems and soft-switching power converters.

Zhongbang Chen was born in China in 1999. He received a Bachelor's degree in Automation from Software Engineering Institute of GuangZhou, GuangZhou, China, in 2017. He is currently pursuing the Master's degree in Control Theory and Control Engineering at Hunan University of Technology. His current research interests include wireless power transfer systems.

Shoudao Huang received the B.Eng. and Ph.D. degrees in electrical engineering from the College of Electrical and Information Engineering, Hunan University, Changsha, China, in 1983, and 2005, respectively. He is currently a Full-Time Professor with the College of Electrical and Information Engineering, Hunan University. His research interests include motor design and control, power electronic system and control, and wind energy conversion systems.